Mass Spectrometry Imaging

Deutsche Ausgabe: DOI: 10.1002/ange.201511691
Internationale Ausgabe: DOI: 10.1002/anie.201511691

Molecular Imaging of Biological Samples on Nanophotonic Laser Desorption Ionization Platforms

*Sylwia A. Stopka, Charles Rong, Andrew R. Korte, Sridevi Yadavilli, Javad Nazarian, Trust T. Razunguzwa, Nicholas J. Morris, and Akos Vertes**

Abstract: *Mass spectrometry imaging (MSI) is a comprehensive tool for the analysis of a wide range of biomolecules. The mainstream method for molecular MSI is matrix-assisted laser desorption ionization, however, the presence of a matrix results in spectral interferences and the suppression of some analyte ions. Herein we demonstrate a new matrix-free MSI technique using nanophotonic ionization based on laser desorption ionization (LDI) from a highly uniform silicon nanopost array (NAPA). In mouse brain and kidney tissue sections, the distributions of over 80 putatively annotated molecular species are determined with 40 μm spatial resolution. Furthermore, NAPA-LDI-MS is used to selectively analyze metabolites and lipids from sparsely distributed algal cells and the lamellipodia of human hepatocytes. Our results open the door for matrix-free MSI of tissue sections and small cell populations by nanophotonic ionization.*

Molecular distributions in cells and tissues, in correlation with anatomical features, can provide insight into disease mechanisms, facilitate clinical diagnosis, and reveal the localization of pharmaceuticals. In recent years, new mass-spectrometry-based technologies have been developed for the spatial mapping of metabolites, lipids, proteins, and xenobiotics in tissue sections.[1,2] Targeted techniques, such as autoradiography and histological staining, require radioactive or fluorophore labeling resulting in a limited number of analytes that can be visualized in a single experiment.[3] In contrast, mass spectrometry imaging (MSI) can simultaneously provide spatial distributions for hundreds of metabolites, lipids, proteins, and drugs in a non-targeted fashion.[4,5]

Among the established vacuum-based ionization methods, secondary ion mass spectrometry (SIMS)[6] and matrix-assisted laser desorption ionization (MALDI)[7–9] have been extensively applied for MSI, single cell, and subcellular analysis. In most implementations, SIMS does not require a matrix and can achieve < 100 nm spatial resolution, however it is known to induce a considerable amount of fragmentation for large molecules. In contrast, MALDI requires the addition of an organic matrix that can contribute to ion suppression and spectral interferences in the low mass range. Emerging atmospheric-pressure MSI techniques, including desorption electrospray ionization (DESI)[10] and laser ablation electrospray ionization (LAESI) allow for direct tissue imaging with minimal sample preparation but typically provide limited spatial resolution.[11]

To overcome the challenges associated with matrix heterogeneity and interferences in the low m/z region, a significant number of matrix-free LDI techniques have been introduced.[12] Despite the large variety of these platforms (surface-assisted LDI (SALDI)),[13] carbon nanotubes,[14] porous alumina,[15] platinum nanoflowers,[16] diamond nanowires,[17] nanostructured gold thin film,[18] and zinc, tungsten, and rhenium oxide nanoparticles[19,20]), only a few of them, for example, desorption ionization on porous silicon (DIOS),[21,22] and nanostructure initiator mass spectrometry (NIMS)[23] have been broadly explored for MSI. In a limited number of applications, other matrix-free techniques, including LDI from laser engineered graphene paper,[24] carbon-substrate-assisted LDI,[25] silica plate imprinting followed by LDI,[26] nanowire-assisted LDI (NALDI),[27] and SALDI,[28,29] were also explored for MSI. The most tested system among these platforms, NIMS, was demonstrated for tissue and cell imaging.[30–33]

Earlier studies showed that silicon nanopost array (NAPA) structures, produced with precise control over the height, diameter, and periodicity of the posts, could be optimized for enhanced LDI yields.[34–37] For example, adjusting the aspect ratio of the nanoposts resulted in extreme sensitivity with a limit of detection in the zeptomole range, and a dynamic range of over three orders of magnitude, whereas imprecisions in the periodicity had negligible influence.[36] The ultratrace detection and quantitation capabilities of NAPA provided insight into metabolic changes in single yeast cells induced by oxidative stress.[38] These features indicate that the NAPA substrate is an appealing candidate for MSI.

In nanophotonic ionization, the geometrical features of the nanostructure are commensurate with the wavelength of the laser light used to induce LDI. This results in a unique interaction between the nanostructure and the laser radiation. The two most important consequences of nanophotonic ionization are the polarization dependence of the ion yield[39] and the ability to adjust the internal energy of the produced ions through the laser fluence.[40] These unique features of NAPA provide opportunities to control the ion

[*] S. A. Stopka, C. Rong, Dr. A. R. Korte, Prof. A. Vertes
Department of Chemistry
The George Washington University
Washington, DC 20052 (USA)
E-mail: vertes@gwu.edu
Dr. S. Yadavilli, Dr. J. Nazarian
Research Center for Genetic Medicine, Children's National Medical Center, Washington, DC 2001 (USA)
Dr. T. T. Razunguzwa, Dr. N. J. Morris
Protea Biosciences Inc. Morgantown, WV 26505 (USA)

Supporting information and the ORCID identification number(s) for the author(s) of this article can be found under http://dx.doi.org/10.1002/anie.201511691.

yield of the LDI process and the internal energy of the produced ions that offer new opportunities in imaging experiments.

To produce larger NAPA surfaces required for MSI, the earlier patterning technology, based on electron-beam lithography, was replaced by deep UV projection lithography, a high throughput nanofabrication method.[37] This nanoprecise fabrication technique produced NAPA substrates that were uniform throughout an entire wafer (ca. 100 mm in diameter), and exhibited heterogeneity only on the submicrometer scale.

Herein we demonstrate the first molecular imaging experiments using LDI-MS from silicon NAPA for the detection and spatial mapping of metabolites and lipids in various biological samples, for example, tissue sections. The ability to selectively target thin cellular features by LDI from NAPA is utilized for the metabolic analysis of lamellipodia. The mechanism of material removal in NAPA-LDI-MSI is illuminated by scanning electron microscope (SEM) observations of the pores in the tissues produced by the underlying nanoposts heated by laser radiation.

To demonstrate MSI capabilities from NAPA, 10 μm coronal sections (0.3 to 0.9 mm anterior from bregma) of mouse brain tissue were transferred by thaw-mounting onto NAPA chips and imaged in positive and negative ion modes (Figure 1). As shown in Figure S1 in the Supporting Information, the mass spectra in both ion modes showed high signal-to-noise ratios with very low interference from the background. After de-isotoping, the negative- and positive-ion spectra contained 163 and 198 different ionic species, respectively. The laser fluence required for desorption of a 10 μm thick sample on a NAPA substrate was approximately 100 mJ cm^{-2}. In comparison, for a 12 μm mouse-embryo section the original version of NIMS needed a laser etching step with 400 mJ cm^{-2} fluence followed by NIMS analysis at 10 mJ cm^{-2}.[23] More recently, the need for laser etching has been eliminated by cutting thinner tissue sections (2–4 μm) and NIMS imaging is performed at around 100 mJ cm^{-2}.[31,41] Overall, the need for thinner sections or higher fluences for NIMS suggests that desorption is more efficient from NAPA structures.

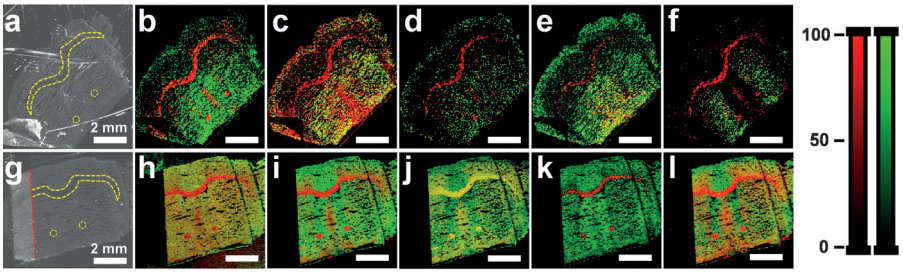

Figure 1. a) Optical image of coronal mouse brain tissue section on a NAPA chip before LDI-MSI. Combined distributions of b) [ST(24:1)−H]$^-$ and [PE(P-38:4)−H]$^-$, c) [octadecenoic acid−H]$^-$ and [PE(P-38:6)−H]$^-$, d) [eicosenoic acid−H]$^-$ and [PE(34:0)−H]$^-$, e) [docosatetraenoic acid−H]$^-$ and [docosahexaenoic acid−H]$^-$, and f) [PE(P-18:2/18:1)−H]$^-$ and [PE(36:4)−H]$^-$ derived from negative-ion spectra and presented on (red) and (green) false color scales, respectively. g) Optical image of coronal mouse brain tissue section on a NAPA chip before LDI-MSI. Red line indicates the edge of the NAPA chip. Composite distributions of h) [cholesterol−H_2O+H]$^+$ and [DG(P-32:1)+H]$^+$, i) [PI−Cer(18:0/18:0)+H]$^+$ and [PC(32:0)+K]$^+$, j) [PC(18:0/16:1)+Na]$^+$ and [PA(38:2)+K]$^+$, k) [PI-Cer(40:0)+H]$^+$ and [PE(P-40:6)+K]$^+$, and l) [PI-Cer(38:0)+H]$^+$ and [PE(38:6)+K]$^+$ from positive-ion spectra presented on (red) and (green) false color scales, respectively.

A total of 80 metabolites and lipids were putatively annotated and spatially mapped from a coronal mouse-brain section (see Table S1 and S2). For example, the negative ion at *m*/*z* 888.6258 assigned as [ST(24:1)−H]$^-$ and [eicosenoic acid−H]$^-$ appearing at *m*/*z* 309.2795 were more abundant in the corpus callosum (CC) and the anterior commissure (aco), whereas the ion at *m*/*z* 718.5453, corresponding to [PE(34:0)−H]$^-$, was localized to the caudoputamen (CP) and the cortex (see panels b–f in Figure 1).

To ascertain that the MSI signal was directly correlated with the NAPA substrate, a brain section was deposited at the interface between the chip and the unprocessed silicon wafer (see panels g–l in Figure 1). The molecular images clearly show that the presence of the NAPA structure is required for signal generation.

To determine the spatial resolution of tissue imaging by NAPA-LDI-MSI, a 10 μm section of the cerebellum was mapped using oversampling with 25 μm step size and a laser fluence of around 100 mJ cm^{-2} (see Figure S2). Anatomical features of the arbor vitae fiber tracts from the granular layers were discernable in the optical microscopy images (see Figure S2a). Molecular imaging on NAPA (Figure S2b) revealed spatial resolution of approximately 40 μm. The main reason behind the modest spatial resolution was the laser focal spot size in the commercial instrument. Based on the high sensitivity provided by the NAPA structures and the uniform post distribution, with better focusing, a submicrometer spatial resolution seems ultimately achievable. Direct comparison with MALDI-MSI (see Table S3) indicates that currently this long-established technique offers better ultimate spatial resolution but the dynamic range of quantitation by NAPA is greater.

Surface characterization of the tissue sections after laser exposure by SEM showed the development of distinct pores (see Figure 2). The pores exhibited average diameters and periodicities of 146 ± 19 nm and 332 ± 36 nm, respectively that closely matched the 150 nm diameter and 337 nm periodicity of the nanoposts. This observation provided insight into the mechanism of ion production from thin tissue sections resting on a NAPA structure. Nanophotonic interactions between the silicon structure and the laser irradiation result in fast heating of the posts.[34,42] The hot tips of the posts induce rapid local evaporation resulting in volatilization of the tissue material. Ionization of adsorbates on NAPA upon laser irradiation has been attributed to the enhanced electromagnetic field in the tip region. Our results

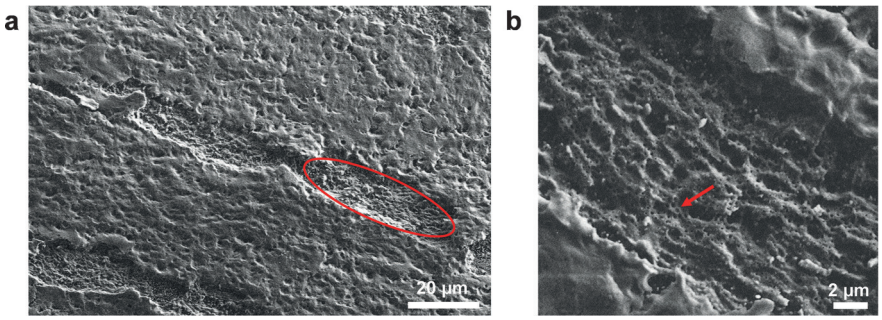

Figure 2. a) An SEM image of a 10 µm thick coronal mouse-brain section on a NAPA chip after exposure to 10 laser pulses per position at a fluence of 100 mJ cm^{-2}. Step size between the exposed areas is 50 µm. The altered tissue as a result of laser desorption in a single pixel is highlighted by a red ellipse. b) Higher-magnification SEM image showing pores (see arrow) generated by tissue removal as a result of the hot nanoposts heated by the laser radiation.

also show the uniformity of ion generation down to submicrometer scale, however owing to the uncontrolled relative position between the nanoposts and tissue features, selective sampling cannot be achieved on that scale.

To investigate the versatility of nanophotonic structures as an imaging platform, another tissue type with higher tensile strength, and cell deposits from an algal culture were subjected to NAPA-LDI-MSI. A 10 µm sagittal mouse-kidney section was mounted onto a NAPA chip and imaged in positive ion mode (Figure 3). Imaging of the algal cells is discussed in the Supporting Information. Localization of certain metabolites and lipids in the kidney section was apparent from higher ion abundances from specific anatomical regions. For example, as shown in Figure 3b, the heme b cation at m/z 616.1771 was detected primarily from the vascular features of the kidney, including capillaries, clearly visible in the composite image in Figure 3e. The ion assigned as $[PE(40:8)+K]^+$ at m/z 826.4779 was mainly localized to the renal medulla and the lipid ion $[PC(32:0)+K]^+$ was detected mainly in the renal cortex (Figure 3c,d). Similar to mouse brain imaging, the mass spectrum from the kidney (see Figure S3) did not show background interferences.

Subcellular variations in composition are masked when chemical analysis is carried out on entire cells. Many cells contain structures known as lamellipodia that are responsible for cell motility and extend from the cell body as an approximately 0.2 µm thin layer of cytoplasm at the front end of a moving adherent cell.[43] Analysis of metabolites and lipids in these thin cellular structures is a largely unexplored field.

To explore the capability of NAPA-LDI-MS for the analysis of lamellipodia, HepG2/C3A human hepatocarcinoma cells were cultured directly on NAPA chips. (Invertebrate neurons had been cultured and analyzed on DIOS chips.[44]) After six days of incubation, SEM imaging revealed the attachment of the cells to the nanoposts (Figure S4). Owing to the large difference in thickness between the cell body and the lamellipodia, at moderate fluences the laser radiation can only heat up the underlying nanoposts for the lamellipodia, and facilitate rapid vaporization of the thin cellular material. (The cell body can also be analyzed at higher laser fluences.) Indeed, observations by SEM after irradiation at a laser fluence of about 24 mJ cm^{-2} revealed small pores where the posts touched the lamellipodia (see Figure 4a). From the lamellipodia, among other ions $[\text{phosphocholine}+H]^+$, $[\text{glucose}+Na]^+$, $[\text{cholesterol-}H_2O+H]^+$, $[TG(50:8)+K]^+$, and $[PE(38:4)+K]^+$ were detected. For clusters of 12 cells, irradiation at a fluence of approximately 24 mJ cm^{-2} gave rise to 27 peaks in the mass spectrum (see Figure 4b) that after background subtraction, de-isotoping, and discounting the molecular adducts corresponded to 13 cellular components.

These results demonstrate the first applications of NAPA-LDI-MS for putative annotation and imaging of over 80 molecular species in animal organ sections and microbial cell deposits. Analysis of 13 metabolites and lipids from lamellipodia was made possible by the selective heating of the nanoposts under these thin structures. These examples show the utility of nanophotonic ion production from biological specimens through the interactions of nanopost arrays and laser radiation. Future work can explore the possibility of selective interactions between nanostructures and cells for

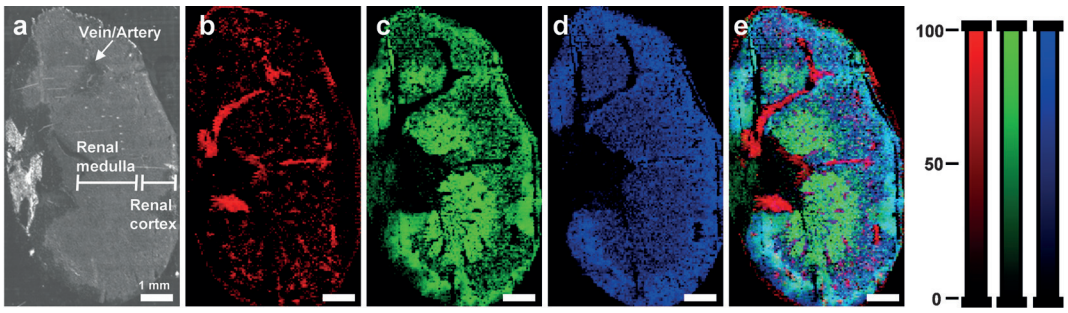

Figure 3. a) Optical image of a 10 µm thick mouse kidney section deposited on a NAPA chip. Spatial distributions of b) $[\text{heme b}]^+$, c) $[PE(40:8)+K]^+$, d) $[PC(32:0)+K]^+$ produced by NAPA-LDI-MSI. The $PE(40:8)+K]^+$ and $[PC(32:0)+K]^+$ correlate with the renal medulla and the cortex, respectively. Veins, arteries, and capillaries are clearly visible in e) the composite plot including all three ions.

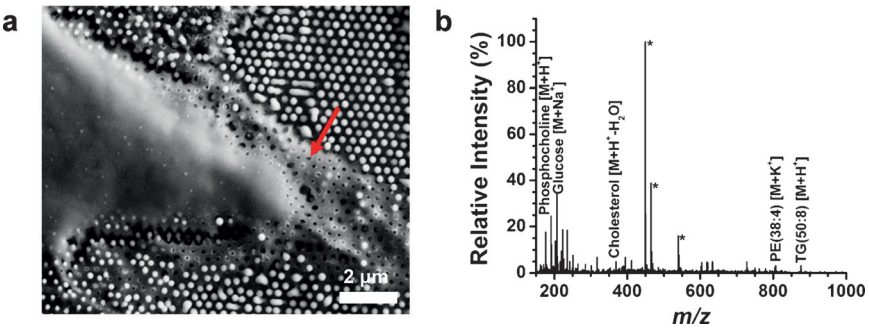

Figure 4. a) SEM image of a HepG2/C3A cell on NAPA, exposed to approximately 24 mJ cm^{-2} laser fluence, with pores (see arrow) in the lamellipodia induced by the irradiated nanoposts. b) Corresponding mass spectrum indicates metabolite and lipid ions originating selectively from the lamellipodia. Background ions from NAPA are marked by *.

molecular analysis and imaging. Molecular imaging of disease biomarkers and drug candidate distributions in tissue sections can also benefit from this matrix free platform.

Experimental Section

Nanofabrication of the NAPA substrate involved deep UV projection lithography and deep reactive ion etching on low resistivity, p-type silicon wafers. The produced nanoposts had dimensions of 150 nm in diameter, 337 nm periodicity, and a height of 1100 nm. Typical imaging chips were 25×25 mm^2 in size and comprised of 5.5×10^9 posts. Biological tissue sections and other samples were transferred onto the NAPA platform for LDI-MS analysis. All experiments were performed using a LTQ-Orbitrap XL mass spectrometer equipped with an intermediate pressure MALDI ion source. The laser focal spot size was approximately 100×80 μm^2, and oversampling was employed for LDI imaging. Additional experimental information is provided in the Supporting Information.

Acknowledgements

This material is based upon work supported by the U.S. Department of Energy, Office of Science, Office of Basic Energy Sciences, Chemical Sciences, Geosciences and Biosciences Division under Award Number DE-FG02-01ER15129 to A.V. S.A.S. is appreciative of the scholarship award from the Achievement Rewards for College Scientists Foundation, Inc.

Keywords: mass spectrometry imaging · silicon nanopost array · small-molecule imaging · tissue section

How to cite: *Angew. Chem. Int. Ed.* **2016**, *55*, 4482–4486
Angew. Chem. **2016**, *128*, 4558–4562

[1] A. Dove, *Science* **2010**, *328*, 920–922.
[2] M. M. Gessel, J. L. Norris, R. M. Caprioli, *J. Proteomics* **2014**, *77*, 71–82.
[3] A. McEwen, C. Henson, *Bioanalysis* **2015**, *7*, 557–568.
[4] A. Roempp, S. Guenther, Y. Schober, O. Schulz, Z. Takats, W. Kummer, B. Spengler, *Angew. Chem. Int. Ed.* **2010**, *49*, 3834–3838; *Angew. Chem.* **2010**, *122*, 3923–3927.
[5] B. Spengler, *Anal. Chem.* **2015**, *87*, 64–82.
[6] S. G. Boxer, M. L. Kraft, P. K. Weber, *Annu. Rev. Biophys.* **2009**, *38*, 53–74.
[7] D. S. Cornett, M. L. Reyzer, P. Chaurand, R. M. Caprioli, *Nat. Methods* **2007**, *4*, 828–833.
[8] T. A. Zimmerman, S. S. Rubakhin, J. V. Sweedler, *J. Am. Soc. Mass Spectrom.* **2011**, *22*, 828–836.
[9] J. Krismer, J. Sobek, R. F. Steinhoff, S. R. Fagerer, M. Pabst, R. Zenobi, *Appl. Environ. Microbiol.* **2015**, *81*, 5546–5551.
[10] J. M. Wiseman, D. R. Ifa, Q. Song, R. G. Cooks, *Angew. Chem. Int. Ed.* **2006**, *45*, 7188–7192; *Angew. Chem.* **2006**, *118*, 7346–7350.
[11] E. R. Amstalden van Hove, D. F. Smith, R. M. A. Heeren, *J. Chromatogr.* **2010**, *1217*, 3946–3954.
[12] N. Bergman, D. Shevchenko, J. Bergquist, *Anal. Bioanal. Chem.* **2014**, *406*, 49–61.
[13] J. Sunner, E. Dratz, Y. C. Chen, *Anal. Chem.* **1995**, *67*, 4335–4342.
[14] S. F. Ren, L. Zhang, Z. H. Cheng, Y. L. Guo, *J. Am. Soc. Mass Spectrom.* **2005**, *16*, 333–339.
[15] R. Nayak, D. R. Knapp, *Anal. Chem.* **2007**, *79*, 4950–4956.
[16] S. Nitta, H. Kawasaki, T. Suganuma, Y. Shigeri, R. Arakawa, *J. Phys. Chem. C* **2013**, *117*, 238–245.
[17] S. Szunerits, Y. Coffinier, R. Boukherroub, *Sensors* **2015**, *15*, 12573.
[18] R. Nayak, D. R. Knapp, *Anal. Chem.* **2010**, *82*, 7772–7778.
[19] T. Watanabe, H. Kawasaki, T. Yonezawa, R. Arakawa, *J. Mass Spectrom.* **2008**, *43*, 1063–1071.
[20] M. C. Bernier, V. H. Wysocki, S. Dagan, *J. Mass Spectrom.* **2015**, *50*, 891–898.
[21] J. Wei, J. M. Buriak, G. Siuzdak, *Nature* **1999**, *399*, 243–246.
[22] S. A. Trauger, E. P. Go, Z. X. Shen, J. V. Apon, B. J. Compton, E. S. P. Bouvier, M. G. Finn, G. Siuzdak, *Anal. Chem.* **2004**, *76*, 4484–4489.
[23] T. R. Northen, O. Yanes, M. T. Northen, D. Marrinucci, W. Uritboonthai, J. Apon, S. L. Golledge, A. Nordstrom, G. Siuzdak, *Nature* **2007**, *449*, 1033–U1033.
[24] K. Qian, L. Zhou, J. Liu, J. Yang, H. Y. Xu, M. H. Yu, A. Nouwens, J. Zou, M. J. Monteiro, C. Z. Yu, *Sci. Rep.* **2013**, *3*, 1415.
[25] C. Li, Z. Z. Wang, A. D. Jones, *Anal. Bioanal. Chem.* **2014**, *406*, 171–182.
[26] D. N. de Oliveira, M. S. Ferreira, R. R. Catharino, *PloS One* **2014**, *9*, e90901.
[27] A. Tata, C. Montemurro, A. M. Porcari, K. C. Silva, J. B. L. de Faria, M. N. Eberlin, *Drug Test. Anal.* **2014**, *6*, 949–952.
[28] V. L. Brown, Q. Liu, L. He in *Mass Spectrometry Imaging of Small Molecules*, *Vol. 1203* (Ed.: L. He), Humana Press, New York, NY, USA, **2015**, pp. 175–184.
[29] C. López de Laorden, A. Beloqui, L. Yate, J. Calvo, M. Puigivila, J. Llop, N.-C. Reichardt, *Anal. Chem.* **2015**, *87*, 431–440.
[30] D. Y. Lee, V. Platt, B. Bowen, K. Louie, C. A. Canaria, C. T. McMurray, T. Northen, *Integr. Biol.* **2012**, *4*, 693–699.
[31] G. J. Patti, L. P. Shriver, C. A. Wassif, H. K. Woo, W. Uritboonthai, J. Apon, M. Manchester, F. D. Porter, G. Siuzdak, *Neuroscience* **2010**, *170*, 858–864.
[32] P. J. O'Brien, M. Lee, M. E. Spilker, C. C. Zhang, Z. Yan, T. C. Nichols, W. Li, C. H. Johnson, G. J. Patti, G. Siuzdak, *Cancer Metab.* **2013**, *1*, 4–4.
[33] M. P. Greving, G. J. Patti, G. Siuzdak, *Anal. Chem.* **2011**, *83*, 2–7.
[34] B. N. Walker, J. A. Stolee, D. L. Pickel, S. T. Retterer, A. Vertes, *J. Phys. Chem. C* **2010**, *114*, 4835–4840.

[35] J. A. Stolee, B. N. Walker, V. Zorba, R. E. Russo, A. Vertes, *Phys. Chem. Chem. Phys.* **2012**, *14*, 8453 – 8471.
[36] B. N. Walker, J. A. Stolee, A. Vertes, *Anal. Chem.* **2012**, *84*, 7756 – 7762.
[37] N. J. Morris, H. Anderson, B. Thibeault, A. Vertes, M. J. Powell, T. T. Razunguzwa, *RSC Adv.* **2015**, *5*, 72051 – 72057.
[38] B. N. Walker, C. Antonakos, S. T. Retterer, A. Vertes, *Angew. Chem. Int. Ed.* **2013**, *52*, 3650 – 3653; *Angew. Chem.* **2013**, *125*, 3738 – 3741.
[39] B. N. Walker, T. Razunguzwa, M. Powell, R. Knochenmuss, A. Vertes, *Angew. Chem. Int. Ed.* **2009**, *48*, 1669 – 1672; *Angew. Chem.* **2009**, *121*, 1697 – 1700.
[40] J. A. Stolee, A. Vertes, *Phys. Chem. Chem. Phys.* **2011**, *13*, 9140 – 9146.
[41] O. Yanes, H.-K. Woo, T. R. Northen, S. R. Oppenheimer, L. Shriver, J. Apon, M. N. Estrada, M. J. Potchoiba, R. Steenwyk, M. Manchester, G. Siuzdak, *Anal. Chem.* **2009**, *81*, 2969 – 2975.
[42] B. N. Walker, J. A. Stolee, D. L. Pickel, S. T. Retterer, A. Vertes, *Appl. Phys. A* **2010**, *101*, 539 – 544.
[43] J. V. Small, T. Stradal, E. Vignal, K. Rottner, *Trends Cell Biol.* **2002**, *12*, 112 – 120.
[44] R. A. Kruse, S. S. Rubakhin, E. V. Romanova, P. W. Bohn, J. V. Sweedler, *J. Mass Spectrom.* **2001**, *36*, 1317 – 1322.

Received: December 16, 2015
Published online: March 1, 2016

